International Journal of Mechanical Sciences 285 (2025) 109816

Contents lists available at ScienceDirect

International Journal of Mechanical Sciences

journal homepage: www.elsevier.com/locate/ijmecsci

Deployment dynamics of fluidic origami tubular structures

Yutong Xia [a,*], Evgueni Filipov [b], K.W. Wang [a]

[a] Department of Mechanical Engineering, University of Michigan, Ann Arbor, MI, 48105, USA
[b] Department of Civil and Environmental Engineering, University of Michigan, Ann Arbor, MI, 48105, USA

ARTICLE INFO

Keywords:
Deployable origami structures
Reconfigurable and inflatable structures
Multistable structures
Dynamics of origami deployment
Pneumatic/fluidic pressurized origami tube
Origami model with panel inertial and elasticity

ABSTRACT

The application of origami in engineering has offered innovative solutions for deployable structures, such as in space exploration, civil construction, robotics, and medical devices, due to its ability to enable compact folding and expansive deployment. Despite its great potential, prior studies have predominantly focused on the static or kinematic aspects of the origami, leaving the dynamic deployment behaviors underexplored. This research addresses this gap by, for the first time, investigating the dynamics of deployment of origami tubular structures actuated by fluidic pressure induced by air or liquids. We introduce a novel dynamic model that incorporates and combines panel inertia and elastic properties, critical for capturing the complex behaviors of origami deployment that rigid kinematic models overlook, as well as the fluidic pressure effects on the structural mechanics and dynamics. Our findings, derived from non-dimensionalized models, reveal the profound influences of the structural and input parameters on the dynamic responses, marking a significant new advancement in origami research. Our study on fluidic origami tubes, where internal pressure is varied, uncovers how the pressurization level and rate affect the transient dynamics and final configuration of the system. The introduction of a space-invariant fluidic pressure, applied as either a step or ramp function, demonstrates the system's sensitivity to pressure adjustments, affecting its stiffness, damping ratio, and transient response. This feature leads to a rich multistability landscape, offering the ability to achieve various stable configurations through input pressure control, and uncovering unique dynamic responses such as snap-through and snap-back actions that have not been observed in the past. All these outcomes and insights are especially valuable in raising awareness of nontraditional behaviors and expanding our comfort zone in origami engineering.

Overall, the research efforts not only propel new understanding of pressure actuated tubular origami's dynamic behaviors but also lay a novel foundational framework for developing origami-based systems for a wide array of applications, which will greatly enhance the design and operational possibilities of reconfigurable and deployable adaptive structures.

1. Introduction

The art of origami, transcending its traditional boundaries, has emerged as a strong foundation for designing complex mechanical structures across a spectrum of applications. This ancient practice of folding, rooted in transforming two-dimensional surfaces into intricate three-dimensional forms, is celebrated for its unique capability to facilitate deployment, reconfiguration, and the enhancement of both geometric and physical attributes of engineered systems. Mathematical approaches and computational tools have been developed for design and kinematic folding [1–6]. Engineering applications of origami span exist over a wide range of scales because most of the characteristics of origami structures are scale independent, from micro- and nanoscale systems [7, 8], to metamaterials [9], and to large scale civil [10,11] and space structures [12–15]. Origami-inspired systems can provide extraordinary mechanical properties, such as auxeticity [16], nonlinear stiffness [17–26], multi-stability [27–34], and programmability [9,35–42]. Because of the enormous interest in this field, there have been immense studies on the kinematics and mechanics of origami structures, with a focus on their static or quasi-static behaviors. Origami-based structures, even designed for static applications, may be subject to dynamic loads from the environment. Recently, some efforts thus have been initiated to expand origami designs for dynamic applications such as acoustic metamaterials [43,44], energy absorption [45,46], impact mitigation [47–49], and vibration control [50–53].

Tubular origami designs have emerged as a compelling approach for

* Corresponding author.
E-mail address: yutoxia@umich.edu (Y. Xia).

https://doi.org/10.1016/j.ijmecsci.2024.109816
Received 31 May 2024; Received in revised form 2 November 2024; Accepted 4 November 2024
Available online 7 November 2024

creating inflatable structures [54–58] that can be deployed, characterized by their significant internal volume expansion from compact forms. These designs are further distinguished by their capability for geometry reprogramming, kinematic reconfigurability [58], and achieving high stiffness-to-weight ratios when aggregated [59]. Recent studies into fluidic origami tubes actuated by air or liquid have unveiled their exceptional versatility, where internal pressurization enables features including adjustable shapes and stiffness [17], multi-stability [22,23], and the capacity for programmable energy absorption [24]. The integration of fluidic systems within these structures is particularly advantageous due to their widespread availability in various engineering contexts [60–62], alongside the simplicity and precision with which they can be managed and manipulated.

The essence of origami lies in its deployment process, necessitating a deeper exploration into its dynamic behaviors to optimize deployment performance characteristics such as speed and smoothness. There have been increasing efforts to address the actuation behaviors [63–70] and dynamic characteristics of origami-inspired deployable structures [71–78]. This surge in studies has begun to unlock and elucidate the complex dynamics underlying their deployment, marking a significant advance in our understanding and application of deployable origami systems. For example, in the deployment of origami sheets [78], and Kresling [71] and Miura origami tubes [73], where initial efforts capitalized on the strain energy from the origami's folded state for actuation. These actuation methods, while conceptually simple, typically offered less controllability and reliability compared to systems employing fluidic pressure mechanisms [65]. On the other hand, while the inflatable fluidic tubular origami with internal pressurization has great potential to enable better deployable structures, their rich dynamics have not been explored or understood.

The objective of this research is to advance the field by investigating the deployment dynamics of origami tubular structures actuated by fluidic pressure from air or liquids. This study comes at a pivotal moment, leveraging the growing interest in the pioneering research aimed at deepening our understanding and pushing the boundaries of deployable origami systems. Focusing on Miura origami tubular structures, we aim to bridge the unexplored knowledge gap. By introducing a novel approach and model consisting of inertial effect and elasticity of the faucets, we reveal dynamic phenomena that have not been captured in traditional quasi-static or kinematic evaluations.

Previous dynamic analyses of origami-inspired structures have primarily concentrated on deformation at the fold creases [63], assuming rigid panels throughout the reconfiguration process. These studies fail to capture panel deformation, which is crucial for understanding the pressurization effect on structures and the dynamic deployment process, and providing manufacturing guidelines. Emerging deployment dynamic analyses using FEM for the entire origami structure [79,80], including creases and panels, often incur high computational costs. Our model strikes a balance between computational efficiency and accurately capturing panel deformation, which paves the way for future dynamic analyses of origami structures.

The methodologies created and new insights generated from this study can be harnessed to design for the desired dynamic responses and features of the deployment process, and the final configuration of origami tubular structures. The research tools and outcomes are especially valuable in raising awareness of new phenomena that have not been observed in the past, and providing guidelines to create origami with design parameters (e.g., material properties) and operating conditions (e.g., pressure level and rate) that will cause or avoid these phenomena. In other words, this basic research is impactful in extending our fundamental knowledge and expanding our comfort zone in origami engineering.

The paper is structured as follows: Section 2 introduces the model formulation for Miura origami tubes subjected to fluidic actuation. Sections 3 and 4 conduct quasi-static analyses to discern the effects of the internal pressure field on the structural behavior of the tubes. In Section 5, we examine the structure's stable equilibria across various pressures and folding stiffness conditions. Dynamic simulations in Section 6 shed light on the structure's snap-through behaviors under different pressurization scenarios. Section 7 discusses the preliminary observations with prototypes and outlines future research directions in experimental investigations. Section 8 concludes our study by highlighting our findings and underscoring the potential for further exploration in the dynamic deployment of fluidic origami structures.

2. Model formulation

In this section, we delve into the development of the origami tube model. In the following subsections, we will discuss in detail: (2.1) model geometric specifications, (2.2) stiffness representation, (2.3) inertia representation, (2.4) model non-dimensionalization, and (2.5) deployment setup, including the external activation force of the system and boundary conditions.

The model embodies the origami tube's inertial characteristics through a mass point system, depicting both the translational and principal rotational inertias for each parallelogram panel within the Miura origami system. Beyond the conventional assumption of rigid panels found in traditional kinematic origami models, our method also employs a combination of bars and hinges to effectively illustrate panel flexibility, enabling the observation of dynamic behaviors stemming from panel deformations. Here, bars represent the in-plane rigidity, whereas rotational springs account for the stiffness out of the plane, associated with panel bending and the folding of creases. The model incorporates a system of nodal forces to simulate the effect of internal fluidic pressure, reflecting the force and moment loadings on the panels.

2.1. Geometry

The Miura origami pattern is created through a sequence of alternating mountain and valley folds, as illustrated in Fig. 1a. This unit is characterized by three distinct geometric parameters: the lengths of two creases (a, b), and the smaller angle between them, referred to as the sector angle (γ), as shown in Fig. 1a. Assuming that folding occurs without any panel distortion, implying that each panel remains entirely rigid during any form of reconfiguration or folding, the Miura origami configuration is thus governed by a single degree of freedom (DOF). Consequently, the three-dimensional (3-D) shape of the entire structure can be defined by specifying one of the internal dihedral angles within a Miura origami unit. In this research, the dihedral angle ρ, as shown in Fig. 1b, is selected to represent the folded state of origami tubes based on the assumption of rigid folding.

2.2. Stiffness

The stiffness of the Miura origami tube is represented through a bar and hinge model, specifically utilizing the N5B8 schema, which positions a node at the center of each panel, as shown in Fig. 2a. This model effectively simulates material properties within its parameters, providing a scalable and isotropic approximation of the system's behaviors, including deformations both within the plane and perpendicular to it. For a comprehensive understanding of the bar and hinge model, readers are referred to references [81–87]. The behavior of the panel within its plane is captured by bar elements, defined by the stiffness formula of $k_s = EA/L$, where E represents the Young's Modulus, L denotes the length of the bar, and A signifies the bar's representative cross-sectional area as elaborated in Eq. (1). The cross-sectional areas for bars on the parallelogram's horizontal, vertical, and diagonal sides are denoted by values A_X,A_Y,A_D, respectively. The thickness of the panel is represented by t, with a and b indicating the lengths of the parallelogram's two sides (as shown in Fig. 1a), and ν representing the Poisson's ratio, with their standard values listed in Table 1. The cross-section areas are calculated by Eq. (1) such that,

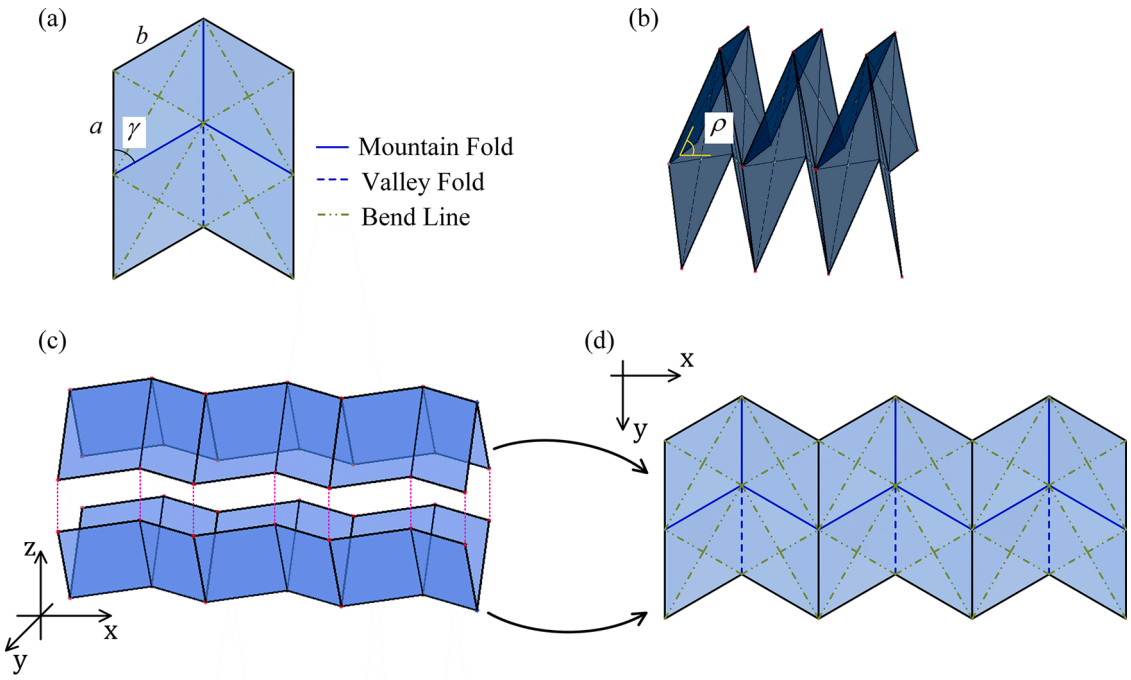

Fig. 1. illustrates components of a Miura origami pattern and the construction of a Miura origami tube. (a) Displays a unit of Miura origami pattern, composed of four panels interconnected by folding lines. The blue dashed lines indicate valley folds and solid lines signify mountain folds, while the green dotted lines represent the bend lines, along which the panels undergo bending deformation. A Miura origami sheet (d) can be formed from three repeated units. (b) Depicts the origami unit (a) in its folded state, highlighting the dihedral angle ρ. The Miura origami tube (c) can be formed by two identical sheets (d), which shows the top view of the unfolded Miura origami sheet in the x-y plane as in (c).

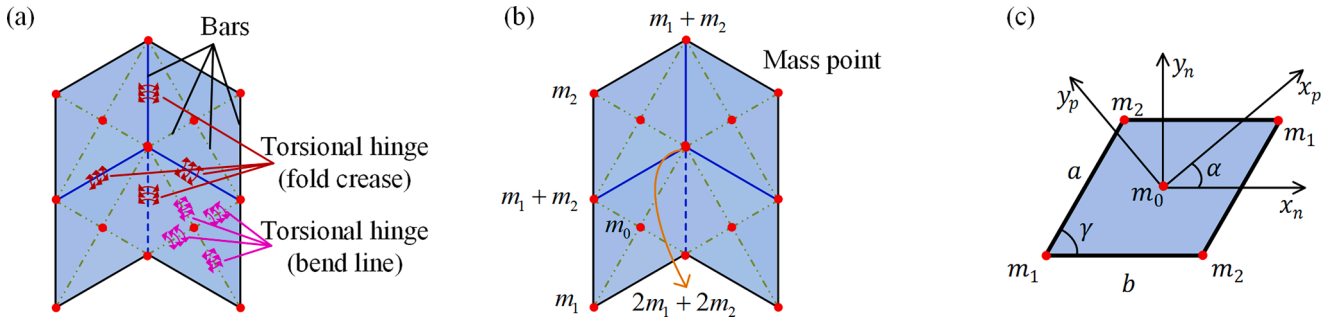

Fig. 2. (a) Presents the bar and hinge model for a Miura origami unit, where circular points symbolize nodes with mass, linked by massless bars (depicted as lines). Torsional springs are installed at the rotation points for the folding creases (including both mountain and valley folds) and at the bending lines (within a panel). (b) The assembled lumped mass system that represents the inertia of a Miura origami unit. (c) The lumped mass system for each panel, which is a quarter of the Miura origami unit. Mass points are placed at the center and four corners of the parallelogram panels. The vector x_n is the axis parallel to the side b of the parallelogram, and y_n is a vector perpendicular to x_n. The vectors x_p and y_p are the principal axes of this parallelogram. The angle between these two coordinate systems is α.

Table 1
Nominal material and geometric properties of the Miura sheet.

Parameter	Nominal value
Young's modulus (E)	$7 \times 10^{10}[N/m^2]$
Poisson ratio (ν)	$0.33[\ -\ ]$
Panel size (side length of the parallelogram)	$0.1 \times 0.1[m]$
Sector angle (γ)	60°
Panel thickness (t)	$0.001[m]$
Panel density (ρ)	$3000[kg/m^3]$

$$A_X = t\,\frac{a^2-\nu b^2}{2a(1-\nu^2)},$$
$$A_Y = t\,\frac{b^2-\nu a^2}{2b(1-\nu^2)}, \tag{1}$$
$$A_D = t\,\frac{\nu\left(a^2+b^2\right)^{3/2}}{2ab(1-\nu^2)}.$$

Eq. (1) illustrates how modifications in panel thickness and parallelogram shape, influence the bar cross-sectional areas and the consequent stretching stiffness.

The out-of-plane stiffness, as a function of the bending angle θ, is calculated by

$$M_b = \theta \cdot k_b = \theta \cdot \left(0.55 - 0.42\frac{2\gamma}{\pi}\right)\frac{Et^3}{12(1-\nu^2)}\left(\frac{D_L}{t}\right)^{1/3}. \tag{2}$$

Within the linear range of hinge deformation, the stiffness per unit length is represented by k_b. Eq. (2) incorporates the sector angle γ, the length of the corresponding diagonal D_L, and the panel thickness t, along with material properties such as Young's modulus E and Poisson's ratio ν. Eq. (2) delineates how the bending angle θ correlates with the reactive torque M_b, which is indicative of panel bending. The bending stiffness of the panel, denoted as k_b, is calculated to be 406 [N] for a Miura panel under the nominal material (aluminum) and geometric conditions listed in Table 1. Note that this k_b corresponds to the shorter diagonal which has a lower stiffness and will be the diagonal that experiences panel bending deformations. In our analysis, we define a stiffness parameter, r_k, equivalent to the ratio of panel bending stiffness k_b to crease folding stiffness k_f. This ratio is maintained above 5, a common characteristic for the majority of folded origami constructions. Our stiffness parametric study focuses on varying the parameters $[r_k,k_f]$ instead of directly manipulating $[k_b,k_f]$.

2.2. Inertia

To represent the inertia of the system in a manner compatible with the bar and hinge model, the parallelogram panels in the Miura origami are replaced by sets of lumped masses. The bars and hinges themselves are assumed to be massless. As a result, the Miura origami structure becomes a simplified finite-DOF structure, as shown in Fig. 2a.

We arrange five mass points with prescribed values at the positions of the five nodes in the N5B8 model to represent the inertia of the panel, as in Fig. 2(b, c). The values of the mass points are denoted by m_0 for the center mass point and m_1 and m_2 for the mass points at the two different corners of the parallelogram. The mass points along each diagonal share the same value. To capture the inertia properties of the panel, we compute the values of the mass points (m_0,m_1,m_2) that make the first and second moments of inertia of the discretized representation equivalent to those of the continuous panel by using

$$\begin{aligned} &m_0 + 2m_1 + 2m_2 = m_c, \\ &I_{mp} = I_c. \end{aligned} \tag{3}$$

In Eq. (3), the value m_c is the mass of the whole panel, I_c is the inertia of the panel, and I_{mp} is the second moment of inertia of the mass point system. The principal moments of inertia I_{x_p} and I_{y_p} of the homogeneous parallelogram panel are derived by

$$\begin{aligned} I_{x_p} &= \frac{m_c}{24}\left(a^2+b^2-\sqrt{\left(a^2+b^2\right)^2-4S^2}\right), \\ I_{y_p} &= \frac{m_c}{24}\left(a^2+b^2+\sqrt{\left(a^2+b^2\right)^2-4S^2}\right), \\ \cos(\alpha) &= \sqrt{\frac{a^2+b^2+\sqrt{\left(a^2+b^2\right)^2-4S^2}-2a^2\sin^2\gamma}{2\sqrt{\left(a^2+b^2\right)^2-4S^2}}}. \end{aligned} \tag{4}$$

In Eq. (4), x_p and y_p refers to the principal axes of the continuum parallelogram, as shown in Fig. 2c. The angle α is between the principal axis x_p and the axis x_n which is parallel with side b of the parallelogram.

$$\begin{aligned} I_i &= m_i\left(|r_i|^2 - r_i r_i^T\right), \\ I_{mp} &= I_0 + I_1 + I_2 + I_3 + I_4. \end{aligned} \tag{5}$$

In Eq. (5), the position of the i^{th} mass point with respect to the origin is defined as r_i, and is used to compute the rotational inertia of the node I_i.The inertia of the full mass point system is derived by summation of the rotational inertias of all the mass points.

When the values of the mass points are selected as

$$\begin{aligned} m_0 &= \frac{2}{3}m_c, \\ m_1 &= m_2 = \frac{1}{12}m_c. \end{aligned} \tag{6}$$

the first and second moments of inertia of the model match those of the parallelogram plate. Thus, the inertia of a panel can be represented by the set of independent mass points with these designated values.

2.3. Non-Dimensional equations of motion

Having established the stiffness and inertia elements of the system, the equations of motion (EOMs) are derived for each DOF of all the nodes by Lagrange's equations, which is

$$\frac{d}{dt}\left(\frac{\partial L}{\partial \dot{x}}\right) - \frac{\partial L}{\partial x} + \frac{\partial D}{\partial \dot{x}} = F_{Ex}. \tag{7}$$

In Eq. (7), the Lagrangian is defined by $L(x,\dot{x}) = V(x) - T(x,\dot{x})$, where $V(x)$ is the strain energy of the system, and $T(x,\dot{x})$ is the kinetic energy. $D(\dot{x})$ represents energy dissipation from damping during both crease folding and panel elastic deformations. F_{ex} represents external load. The nodal position is defined as x, and the nodal velocity is $\dot{x}$. In this bar and hinge model, if no constraints are imposed on the structure, each node will have three degrees of freedom. More detailed expressions of the terms in Eq. (7) are summarized in the Appendix.

We perform non-dimensionalization to the EOMs. The general form of the EOM for a DOF u_i is

$$\overline{m}_i\ddot{u}_i + \sum_{p=fold}\left(\overline{F}_{f_p} + \overline{F}_{df_p}\right) + \sum_{q=bend}\left(\overline{F}_{b_q} + \overline{F}_{db_q}\right) + \sum_{r=bar}\left(\overline{F}_{s_r} + \overline{F}_{ds_r}\right) = \overline{F}_{ex}, \tag{8}$$

in which u_i is the i-th non-dimensionalized nodal displacement. In Eq. (8), the summation over $p = fold$ refers to all the fold creases that are related to this node; the summation over $q = bend$ refers to all bend lines at this node; the summation over $r = bar$ refers to all the bars that are connected to this node. The forces $\overline{F}_{f_p}$ and $\overline{F}_{b_q}$ refer to the non-dimensional nodal forces at this node generated by the p-th folding crease and the q-th bending line respectively. The force $\overline{F}_{s_r}$ is the non-dimensional force from panel stretching represented by deformation of r-th bar. The non-dimensional nodal forces generated from the damping are $\overline{F}_{df_p}$, $\overline{F}_{db_q}$ and $\overline{F}_{ds_r}$, for the p-th folding crease, the q-th bending line, and the r-th bar respectively. By expanding Eq. (8), we can get the detailed expression, which is

$$\overline{m}_i\ddot{u}_i + \overline{k}_f\overline{L}_f\sum_{p=fold}\left(\frac{\partial\theta_p}{\partial u_i}\left(\theta_p-\theta_{p0}\right) + \frac{\overline{c}_f}{\overline{k}_f}\frac{\partial\theta_p}{\partial u_i}2\zeta_0\dot{\theta}_p\right) + \overline{r}_k\overline{k}_f\overline{L}_b\sum_{q=bend}\left(\frac{\partial\theta_q}{\partial u_i}\theta_q + \frac{\overline{c}_b}{\overline{r}_k\overline{k}_f}\frac{\partial\theta_q}{\partial u_i}2\zeta_0\dot{\theta}_q\right) + \sum_{r=bar}\left(\frac{\overline{L}_r-\overline{L}_{r0}}{\overline{L}_r}\frac{\partial\overline{L}_r}{\partial u_i} + \overline{L}_r\frac{\partial\dot{\overline{L}}_r}{\partial u_i}2\zeta_0\dot{\overline{L}}_r\right) = \overline{F}_{ex}. \tag{9}$$

The area of the parallelogram is defined as S.

The second moment of inertia of the mass point system in the principal directions of the continuum parallelogram is calculated by

The detailed derivations of Eq. (9) from Eq. (8) are provided in the Appendix. As for the external load $\overline{F}_{ex}$, in this study, the deployment of fluidic Miura origami tube is driven by the applied fluidic field inside the tube. Here we assume a space-invariant fluidic field and use nodal forces at the three vertices of each triangular element of a facet to represent the

Table 2
Non-dimensionalization parameters.

Scales	ND parameters
Mass	$\overline{m} = m_i/m_0\ (i = 0,1,2)$
Length	$\overline{L_i} = l_i/a\ (i = p,q,s)$
Time	$\tau = \omega_0 t$
Stiffness	$\overline{k_i} = k_i/EA_{bar}\ (i = f,b)$
	$\overline{r}_k = \overline{k}_b/\overline{k}_f$
Damping	$\overline{c_i} = c_i/a^2 c_{vs}\ (i = f,b)$

force from the internal fluidic field. When the three nodal forces all take on value as $\overline{P_i S_i}/3$ with orientation perpendicular to the facet pointing to the outside of the tube, the first and second moments of the nodal forces match those of the pressure load.

All the parameters and the variables are non-dimensionalized with the parameters found in Table 2. In this table, m_0 is the mass of the central node in the parallelogram panel. The mass-related variables (m_0, m_1,m_2) are non-dimensionalized by m_0. The crease length a depicted in Fig. 1a is used to non-dimensionalize the length-related variables (lengths of folding creases, bending lines, and bar elements). The variable τ is the non-dimensional time, and ω_0 is defined by $\omega_0 = \sqrt{\frac{E \cdot A_D}{a \cdot m_0}}$, in which A_D is the cross-section area of the bar along the diagonal of the parallelogram as in Eq. (3). We introduce a stiffness parameter $\overline{r}_k$, which is the stiffness ratio between panel bending and crease folding. The damping coefficient of torsional springs are non-dimensionalized by the viscous damping coefficient c_{vs} of bar deformation. The damping ratio is defined by $\zeta_0 = \frac{a c_{vs}}{2 m_0 \omega_0}$.

2.4. Deployment setup

In this study, we constructed a 3-unit origami tube with two identical Miura origami sheets, as shown in Fig. 3(a, b, c). We close off both ends of the origami tube, immobilizing the axial movement at the left end while allowing the other (right) end the freedom to move. To model the immobilized end, node 15 is fully constrained in all directions, while nodes 1, 8, and 22 are restricted in axial (x-direction) movement. The node numbering is illustrated in Fig. 3(b, c). The structure begins in a partially folded state, represented by 33.2% of its total deployable extent as depicted in Fig. 3d, and is gradually deployed through the application of internal pressure. The degree of deployment is quantified by comparing the axial projection length of the tube, L_{ax}, to its length when completely unfolded, as shown in Fig. 3e.

We operate under the assumption that the fluidic pressure within the tube remains space-invariant throughout the deployment, addressing both quasi-static and dynamic deployment phases. The quasi-static deployment is detailed in Section 3, while discussions on dynamic deployment span Sections 4 to 6.

3. Quasi-Static deployment

Utilizing the non-dimensionalized equations of motion, this section initiates the deployment study of the Miura origami tube through quasi-static analysis. This initial effort aims to elucidate the effects of internal fluidic pressure magnitude and structural stiffness on the tube's configuration.

Our quasi-static examination investigates how different pressure levels $\overline{P}$affect the tube's unfolding, considering variations in stiffness parameters $(\overline{r}_k, \overline{k}_f)$. The deployment state is determined by the balance between pressure-induced forces and the reactive forces of the structure. Corresponding to each set of stiffness parameters, represented as different curves in Fig. 4, we methodically increase pressure in steps, iteratively searching for a force-balanced configuration using the incremental and iteration method. With each step, the structure advances from its previously balanced state under escalating pressures, beginning from its initial, undeformed state.

Here we explain the incremental and iteration method in detail. For every scenario defined by specific stiffness parameter set, pressure is gradually raised in distinct steps. During each, we engage in an iterative process to identify a force-equilibrium state. Consequently, the structure progressively adjusts from the stable configuration r_{n0} from its last step to face higher pressure in the next, initiating from the resting state of deployment. The structure configuration numerically converges after several iterations, where we use $\overline{U} = \overline{K}^{-1}[\overline{F}_{ex}(\overline{P}) - \overline{F}_{in}]$ to equilibrate the resultant reactive force, where $\overline{U}$is the nodal displacement; $\overline{K}$ is the stiffness matrix; $\overline{F}_{ex}(\overline{P})$ is the external load from fluidic field and is a function of pressure magnitude $\overline{P}$ (note that the word *external* here refers to loads applied onto the numerical model, rather than the location of pressure within the tube); $\overline{F}_{in}$is the internal reactive force from panel and crease deformation. The structure takes on an updated configuration $\overline{r}_{n,i} = \overline{r}_{n,\ (i-1)} + \overline{U}$ in the i th iteration. Because the external load from

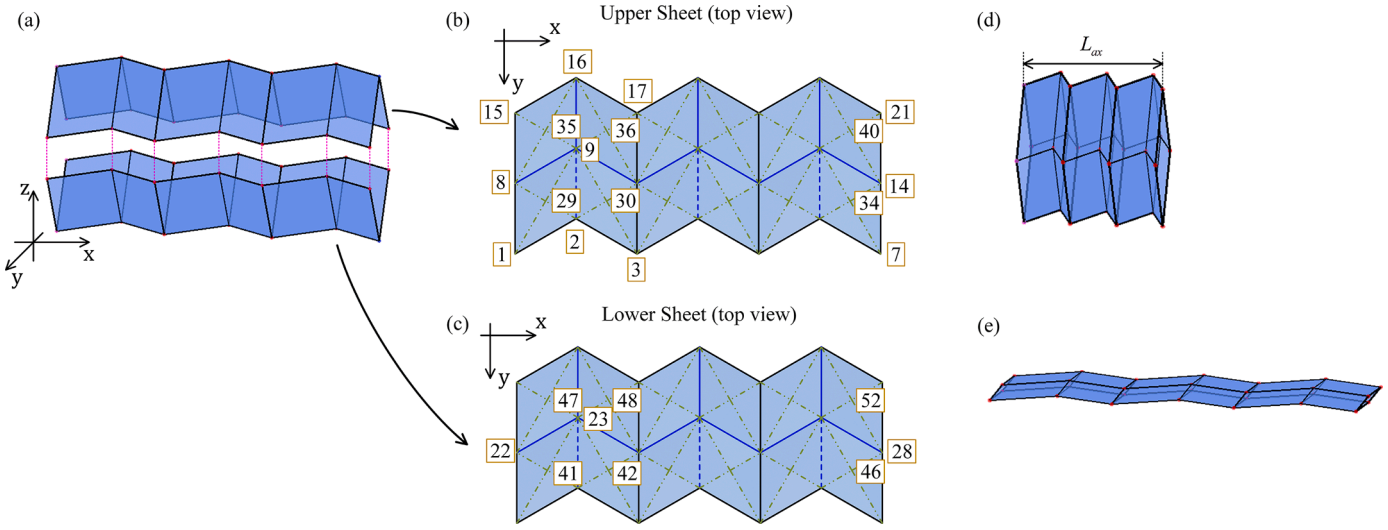

Fig. 3. (a) A 3-unit Miura origami tube consists of two identical Miura origami sheets, the upper sheet (b) and the lower sheet (c). Numbers in yellow blocks in (b, c) represent the node numbering in the upper and lower sheets. (d) Shows a partially folded Miura origami tube. L_{ax} is defined to be the length of axial (x direction) projection of the origami tube. In the following sections, we will describe the deployment extent or deployment stage using the ratio in percentage of the deployment length L_{ax} over the axial length of the fully-deployed, flat configuration.

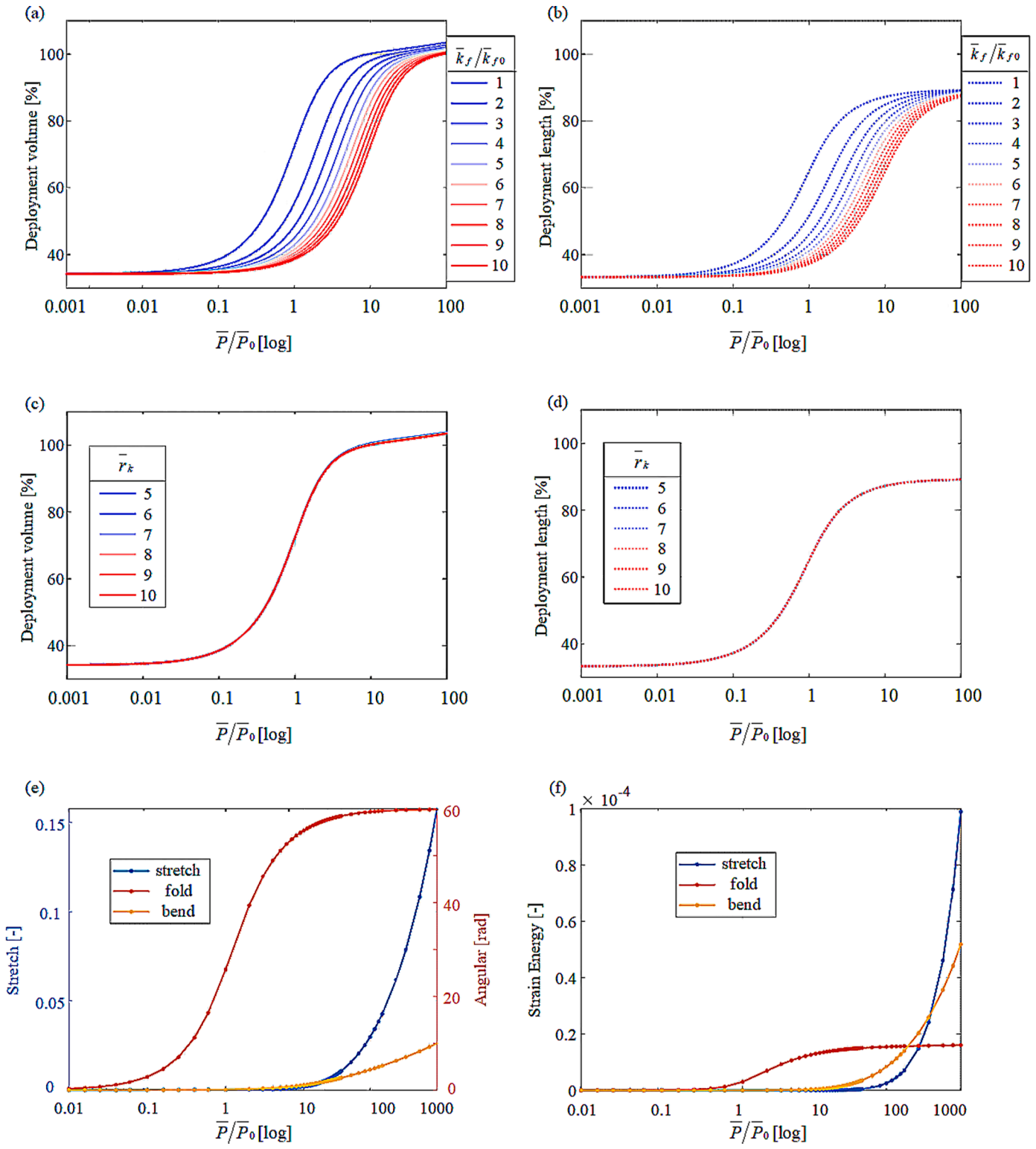

Fig. 4. (a-d) The quasi-static deployment extent of the origami tube versus pressure for different folding stiffness $\bar{k}_f$ and stiffness ratios $\bar{r}_k$. The pressure is in log scale as shown by the lower x-axis. The stiffness ratio in (a, b) is constant at $\bar{r}_k = 10$, and the folding stiffness in (c, d) is constant at $\bar{k}_f/\bar{k}_{f0} = 1$. The deployment extent is described by the volume (a, c) and the end-to-end length (b, d), which are represented by the groups of solid and dotted lines respectively. (e) The deformation of the structural elements, including the panel stretching deformation represented by bar strain, and the crease folding and panel bending deformations represented by angular displacement at hinges and folding creases respectively. (f) The strain energy decomposed into the energy from panel stretching and bending deformation, and the crease folding deformation.

pressure is always perpendicular to the panels, the term $\bar{F}_{ex}$ is updated after each iteration when the configuration $\bar{r}_n$ changes. The internal reactive force $\bar{F}_{in}$is also iteratively updated through the process. For better presentation and illustration, in the rest of the paper, we normalize the applied pressure $(\bar{P})$ using $(\bar{P}/\bar{P}_0)$, where $\bar{P}_0 = 3.8 \times 10^{-6}$.

In Fig. 4a, the transition from blue to red in the curves denotes tubes with increasingly stiffer folding creases, exhibiting a common pattern where higher pressure leads to a greater deployment extent. The volume of deployment shown in Fig. 4a can surpass the maximum volume predicted by rigid folding assumptions under substantial pressure, suggesting that tubes capable of panel elastic deformation can undergo significant inflation. Despite the pressure $\bar{P}/\bar{P}_0$ applied, the maximum extension in terms of axial length, as seen in Fig. 4b, remains at approximately 89%, matching the length at the state of maximum volume. This indicates that upon reaching its maximal length, the tube's extension ceases, regardless of further pressure increases; instead, the tube's volume expansion results from panel stretching rather than elastic deformation at the creases, as illustrated by the strain energy patterns in Fig. 4(e) and (f).

At lower pressure levels, the primary contributions to deformation and strain energy are from the folding of pattern creases, with minimal panel stretching or bending, signifying initial deployment stages. As pressure escalates, the length plateaus near 89%, while volume begins to surpass its theoretical maximum. The data and strain energy graphs reveal a plateau in crease folding deformation and its associated energy, whereas stretching deformation and its energy sharply increase, pointing to inflation rather than further deployment. Furthermore, Fig. 4a comparisons suggest that structures with greater folding stiffness $\bar{k}_f$ require higher pressures for similar deployment extents compared to those with lower $\bar{k}_f$. Conversely, the stiffness ratio $\bar{r}_k$ does not influence deployment, as almost no panel deformation is observed during quasi-static deployment, as depicted in Fig. 4(c) and (d).

4. Influence of pressure field on structural properties

Building on the quasi-static deployment analysis discussed in Section 3, this section presents numerical simulations to explore the dynamics of the deployment process. We will demonstrate dynamic deployment behaviors under various pressure magnitudes and examine how the pressure field inside the origami tube can influence its structural properties and, consequently, its dynamic behaviors.

We model the application of pressure through a step input for these simulations. Fig. 5a illustrates the time progression of the dynamic deployment for a structure characterized by specific stiffness parameter set as $[\bar{r}_k = 10, \bar{k}_f/\bar{k}_{f0} = 10]$ and damping coefficients $[\bar{c}_b/\bar{r}_k \cdot \bar{k}_f, \bar{c}_f/\bar{k}_f] = [2.6, 1.3] \times 10^5$. The effect of the internal fluidic field on both the deployment extent and the transient dynamics is illustrated in Fig. 5a. At lower pressures, the structure demonstrates highly damped behavior, indicated by the smooth, blue curves. As pressure increases, the system dynamics evolved and become less damped. When $\bar{P}/\bar{P}_0 = 100$, an overshoot in the axial direction is observed, leading the tube to temporarily extend beyond its equilibrium state before settling without significant oscillation at the pressure-adjusted state. With further increases in pressure, the structure begins to exhibit more pronounced axial oscillations.

The transition of the damping behavior with increasing pressure underscores how the internal fluidic field adjusts the structural stiffness, affecting the system's damping ratio and deployment dynamics. This relationship is further elucidated through eigenvalue analysis on the structure's stable equilibria at different pressure levels. Fig. 5b shows the natural frequency and damping ratio of the first mode of the origami structure, which corresponds to the folding and unfolding mode according to the modal analysis. The rise in natural frequency and reduction in damping ratio with increasing internal pressure indicates the tunable structural behaviors via fluidic pressure controls.

To deepen our understanding of the structural characteristics, we undertake an eigenvalue analysis on structures possessing varied stiffness across different pressure scenarios. Previous research on the dynamics of origami sheet deployment revealed that the structural folding stiffness $\bar{k}_f$ exerts a more pronounced effect on deployment outcomes than the stiffness ratio between the panel bending stiffness and crease folding stiffness [78]. Hence, this analysis focuses on folding stiffness $\bar{k}_f$ as the primary variable. Fig. 6(a, b) presents the natural frequency and the damping ratio from an eigenvalue study, mapping various folding stiffness and pressure conditions. Each point on the contour plots Fig. 6(a, b) corresponds to a stable equilibrium for a structure at a specific folding stiffness and pressure level, where structures with more flexible folding creases reach larger deployment extents under the same pressure value; while for the same folding stiffness, high pressure will cause larger deployment extents. Fig. 6b illustrates the effective damping ratio, with white areas denoting overdamped systems and colored areas indicating underdamped systems. Dynamic simulations for four distinct parameter sets are documented, showcasing the deployment process across these scenarios in Fig. 6c. Points chosen from the overdamped area result in a gradual deployment process; points from the underdamped area exhibit overshoot and potential oscillations; whereas, points at the boundary between overdamped and

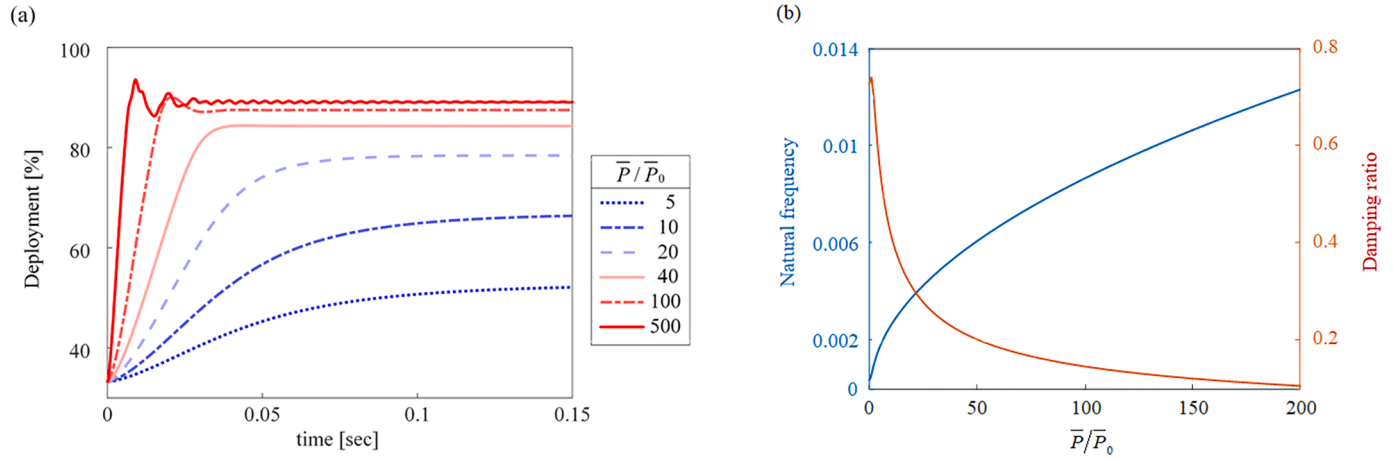

Fig. 5. (a) Time history of the dynamic deployment process for varied pressure magnitudes. The state of deployment is represented based on the maximum axial length of the tube. (b) The first mode natural frequency and damping ratio vary with internal pressure magnitude. The stiffness parameters of the structure in both (a) and (b) are $[\bar{r}_k = 10, \bar{k}_f/\bar{k}_{f0} = 10]$.

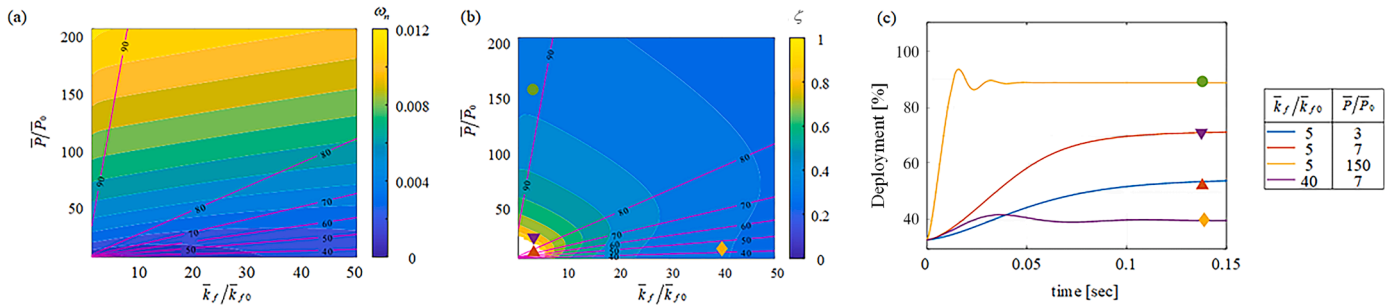

Fig. 6. This figure presents the variations in the first mode natural frequency ω_n(a) and damping ratio ζ (b) across a range of stiffness parameters and internal pressure levels for a Miura origami tube. The red lines overlaid in parts (a) and (b) indicate the different extension lengths based on the pressure/stiffness parameters. The stiffness parameter variation is plotted along the x-axis, while pressure magnitude variations are shown on the y-axis. Part (c) displays the dynamic deployment process over time for four selected sets of (stiffness, pressure) parameters from part (b).

underdamped areas lead to rapid and smooth deployment, akin to a critically damped system. This variation in structural behavior under different pressures hints at the ability to tailor deployment performance through pressure adjustment in concurrent with structural modification. Although this eigenvalue analysis concentrates on the stable equilibria, it offers valuable insights for parametrically designing structures to achieve specific dynamic deployment behaviors.

5. Multiple stable Equilibria

In addition to the effects on structural stiffness and damping discussed in Section 4, the pressurization also can qualitatively influence the deployment behaviors. This section examines how the multi-stability landscape of the fluidic origami tube leads to distinct dynamic deployment processes, focusing on the effects of pressure magnitude and structural stiffness coefficients. More specifically, we explore (5.1) the effects of pressure magnitude and (5.2) the influence of stiffness coefficients on the multi-stability landscape and the system's dynamics.

To quantify the deviation of the tube configuration relative to a rigid-folded baseline, we utilize the average nodal deviation δ. This measure compares the deformation of the system against a rigid-folded model, assuming no elasticity. We use a rigid-folded configuration with the same axial length L_{ax} as a reference point (illustrated as the blue configuration in Fig. 7f), and then we compute the deviations between corresponding nodes from the dynamically deployed (shown in yellow in Fig. 7f) and the baseline rigid-folded configurations, indicated by pink arrows. The deviation δ is calculated as the mean value across all paired nodes: $\delta = \frac{1}{N}\sum_i |\bar{r}_i - \bar{r}_{ir}|$, where N is the number of total nodes in the origami tube, $\bar{r}_i$ is the nodal position from numerical simulation (yellow configuration in Fig. 7f), $\bar{r}_{ir}$ is the nodal position from corresponding configuration under rigid assumption (blue configuration in Fig. 7f).

For the origami tube characterized by specific stiffness parameters $[\bar{r}_k = 10,\ \bar{k}_f/\bar{k}_{f0} = 1]$ and damping coefficients $[\bar{c}_b/\bar{r}_k\cdot\bar{k}_f,\ \bar{c}_f/\bar{k}_f] = [7.8, 3.9] \times 10^4$, we observe three distinct categories of deployment behaviors based on the pressure amplitude:

(1) Under low pressure ($\bar{P}/\bar{P}_0 < 12$), the structure undergoes expansion (Fig. 8c), exhibits axial oscillations (Fig. 8d), and stabilizes close to its initial rigid-folded configuration (Fig. 8e). The average nodal deviation, as illustrated in Fig. 8b, remains minimal throughout the deployment, indicating little deviation from the rigid-folded state. As pressure increases, so does the deployment extent of the final configuration, as evidenced by the comparison between dashed and dotted blue lines in Fig. 8a. Additionally, within this pressure range, both the oscillation frequency and structural stiffness are found to increase with the pressure.

(2) At normalized pressure $\bar{P}/\bar{P}_0$ within the range of [12,30], the structure undergoes a snap through to a significantly distorted state with pronounced global bending, shown in Fig. 8(f-h). This drastic change in behavior is highlighted in Fig. 8b, where the deviation δ spikes, indicating that the structure deviates substantially from the expected rigid-folding path and maintains a distorted configuration throughout the dynamic simulation without further deployment.

(3) For pressure $\bar{P}/\bar{P}_0$ exceeding 30, the structure initially snaps to a highly distorted state similar to the second group but then reverts to a less distorted or nominal form. This snap-back is depicted in Fig. 8i, and the transient stretched-out configuration is shown in Fig. 8j, marked by a blue square in Fig. 8a, indicating a deployment state flatter and more extended than the maximum volume state seen in Fig. 4a. This results in uneven deployment across the tube's three units and a comparatively higher average nodal deviation δ, as shown in Fig. 8b. Eventually, the structure settles near its original rigid state with a low δ, as demonstrated in Fig. 8k.

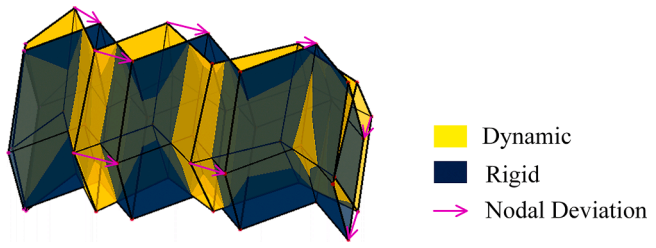

Fig. 7. The blue configuration refers to the state of the origami tube under rigid-panel assumption, where the only deformation happens at the fold lines. The yellow configuration refers to the state simulated using the model proposed in Section 2, where the panel flexibility is considered. The pink arrows show the node-wise displacement between the dynamic configuration and the corresponding rigid configuration.

To elucidate the three distinct deployment behaviors observed, we investigate the origami tube's capacity for multiple stable equilibria. We explore the different equilibria through an energy minimization approach where a specific internal pressure $\bar{P}/\bar{P}_0$ is applied, and the structure is allowed to settle into a stable equilibrium from a perturbed initial configuration $\bar{r}_{n0}$. Through iterative application of $U = \mathrm{K}^{-1}(\mathrm{F_{ex}} - \mathrm{F_{in}})$ to balance the reactive forces, the configuration is updated by $\bar{U} = \bar{K}^{-1}[\bar{F}_{ex}(\bar{P}) - \bar{F}_{in}]$. This method yields two distinct stable equilibria. In the first, initiating from the tube's rigid-folded state, the process leads to a stable configuration characterized by minor panel deformation and negligible nodal deviation. The second stable equilibrium starts from a condition markedly different from the rigid-folded state—derived from the transient analysis phase—and results in significant structural distortion.

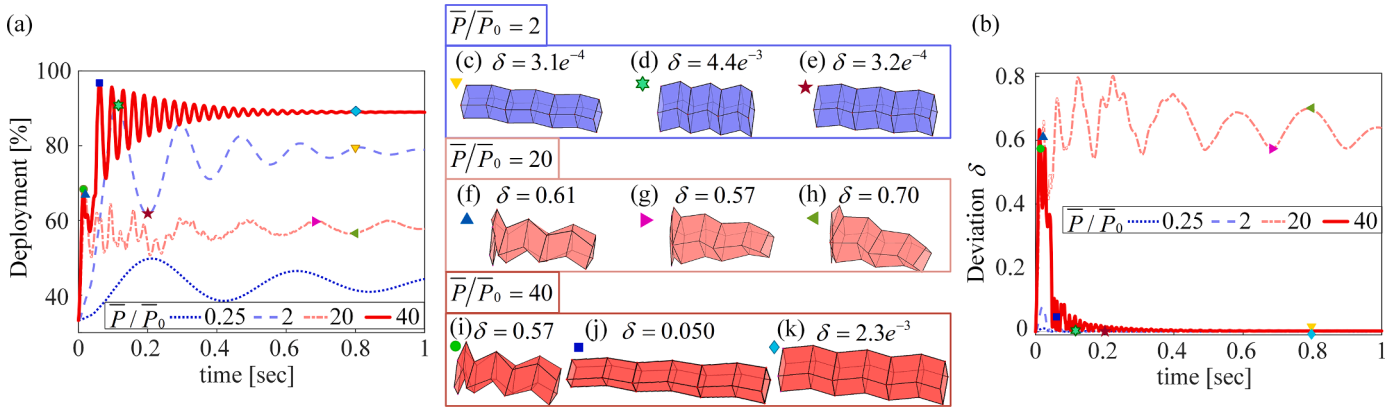

Fig. 8. (a) Illustrates the temporal progression of dynamic deployment under varying pressure magnitudes, applied in a stepwise manner. Specific stages of deployment are captured in snapshots (c) through (k) for different pressure levels. (b) Depicts the temporal evolution of average nodal deviationδ across different pressure magnitudes. The structural analysis is based on predefined stiffness parameters $[\bar{r}_k = 10, \bar{k}_f/\bar{k}_{f0} = 1]$.

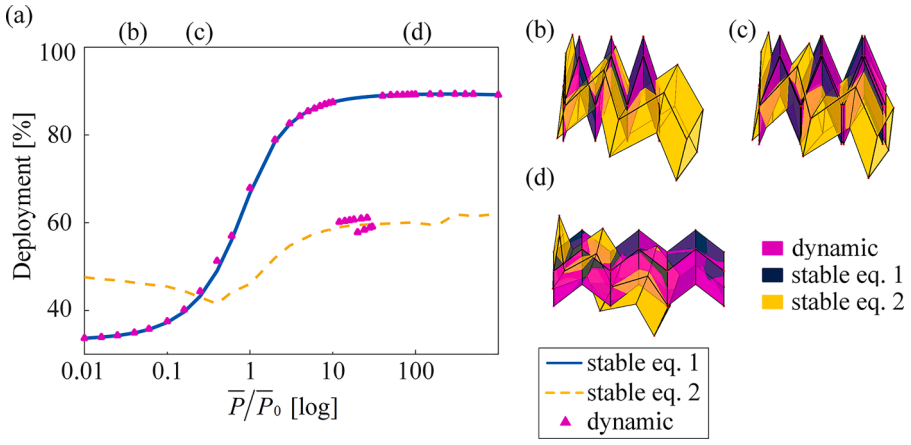

Fig. 9. (a) The two stable equilibria and the settled dynamic configuration of the structure under different magnitudes of pressure are shown with respect to the length of the tube axial projection. (b-d) The comparison among the two stable equilibria and the settled dynamic configuration in different colours under pressures of $\overline{P}/\overline{P}_0 = [0.04,\ 0.25,\ 100]$ respectively.

Moreover, the structure's inherent properties, alongside the pressure field, play pivotal roles in shaping the multistability landscape. The subsequent sections will investigate how both pressure and structural stiffness affect this landscape of multiple stable states.

5.1. *Influence of pressure field on stable equilibria*

In this section, we adjust the internal pressure magnitude to analyze the structure's stable equilibria, both quasi-statically and dynamically. Fig. 9a shows the existence of two stable equilibria across the range of internal pressure examined. We computed these equilibria using the incremental and iterative method outlined in Section 3, starting from varied initial states. The first stable equilibrium was computed by initializing with the configuration under the rigid-panel assumption, where the structure undergoes greater deployment as pressure increases. For the second equilibrium, we used a distorted configuration derived from a settled dynamic simulation as the initial state. In this case, the deployment length in the x-direction initially decreases before increasing again, due to global bending in the y and z directions. Under certain pressure $\overline{P}/\overline{P}_0 \leq 0.4$, the structure bends and rotates transversely (as depicted in Fig. 9(b, c)), shortening the axial projection length. Beyond this pressure range when $\overline{P}/\overline{P}_0 > 0.4$, the second equilibrium no longer bends additionally but extends in length with increasing pressure.

Though dynamic simulation, we generate the final settled configuration as illustrated by the pink triangle-shape points shown in Fig. 9a. The structure aligns with and remains near the first equilibrium path after deployment for pressure $\overline{P}/\overline{P}_0 < 12$. Within the pressure range of [12,30], the tube dynamically settles into the highly distorted second equilibrium. This transition occurs because the initial stepwise application of fluidic pressure surmounts the energy barrier between the two equilibria, prompting the structure to snap into the second stable state. For pressures exceeding 30, the structure initially snaps into this second equilibrium but subsequently returns to the first equilibrium, indicating that the applied fluidic pressure is sufficiently high, allowing the structure to snap through and then back during its oscillatory motion.

5.2. *Influence of stiffness on stable equilibria*

Given that both the pressure field and structural stiffness influence the energy barrier the structure must overcome to snap through, we conduct an in-depth analysis on structures of varying stiffness subjected to different pressure scenarios. Reflecting on the findings from Section 5.1 regarding pressure fields, Fig. 10(a-d) selects specific pressure magnitudes that induce snap-through or snap-back responses in the structure, contingent on certain stiffness values.

Conversely, Fig. 10(c, d) illustrate that the ratio of panel bending to crease folding stiffness scarcely affects the equilibria shapes. Altering panel bending stiffness doesn't significantly affect dynamic deployment, suggesting a stable equilibrium is maintained throughout the deployment process.

Fig. 10e integrates both structural stiffness and pressure factors, with

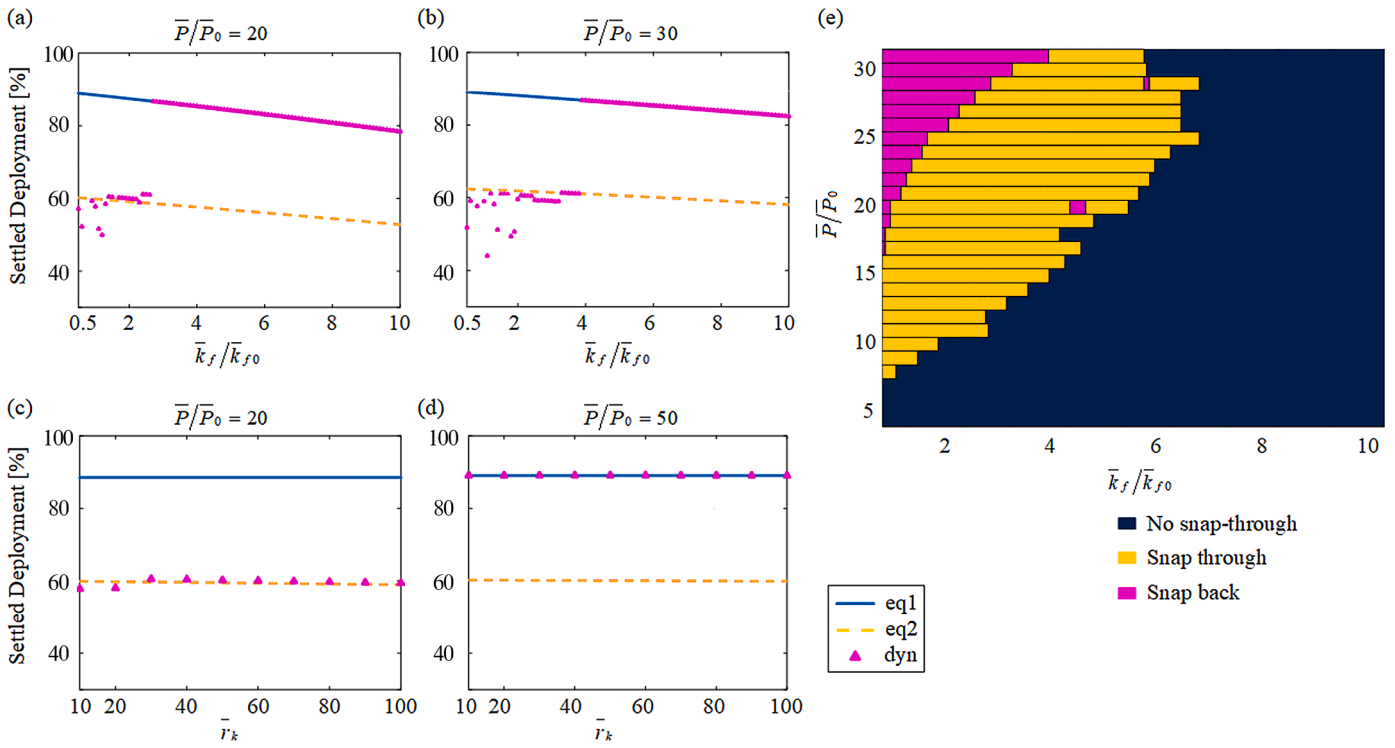

Fig. 10. (a, b) The two stable equilibria and the settled dynamic configuration of structure with different folding stiffness with pressures of $\overline{P}/\overline{P}_0 = [20, 30]$ respectively. The stiffness ratio is kept constant at $\bar{r}_k = 10$. (c, d) The two stable equilibria and the settled dynamic configuration of structure with different stiffness ratios with pressures of $\overline{P}/\overline{P}_0 = [20,\ 50]$ respectively. The folding stiffness is kept constant at $\bar{k}_f/\bar{k}_{f0} = 1$. (e) The contour plot of the dynamic deployment behaviours of structures with different folding stiffness under varied pressure magnitudes.

each color block representing a structure's dynamic deployment behavior under specific stiffness and pressure levels. The horizontal axis aligns with Fig. 10(a, b), showing structures with softer creases likely to snap through at certain given pressure. Vertically, the plot indicates that structures with constant folding stiffness exhibit regular deployment with minimal distortion at lower pressures (dark blue blocks), transitioning to a distorted equilibrium upon pressure increase (yellow blocks). At sufficiently high pressures, structures snap through twice, settling into a regular, less-distorted state (magenta blocks), with critical pressure thresholds rising as folding stiffness increases, as also observed in Fig. 10(a, b). This demonstrates that dynamic deployment behaviors and stable equilibria are influenced by modifying origami tube stiffness, enabling tailored deployment processes through specific stiffness and pressure settings.

6. Deployment dynamics via ramp input

In Sections 4 and 5, we modeled the application of pressure as a step function. In this section, however, we transition to employing a ramp function for pressurization. We will demonstrate that with the same final pressure, varying the pressurization rate significantly alters the dynamic deployment behavior. Given different pressurization rates, the origami tube can achieve either smooth deployment or exhibit snap-through and snap-back behaviors. This contrasts with the previous section, where the deployment was solely determined by the pressure magnitude.

We define t_0 as the duration required to achieve the target pressure magnitude. For this study, we pressurize the system to $\overline{P}/\overline{P}_0 = 20$where previously identified distorted deployments occurred. We then adjust t_0, shown in Fig. 11b, to apply pressure at varying rates and conduct dynamic analysis accordingly. When pressure is introduced swiftly, specifically at rates exceeding $t_0 \leq 5$ ms, pronounced distortion is observed. In these instances, the structure undergoes a snap through to the second stable equilibrium, halting further deployment, as depicted in Fig. 11d.

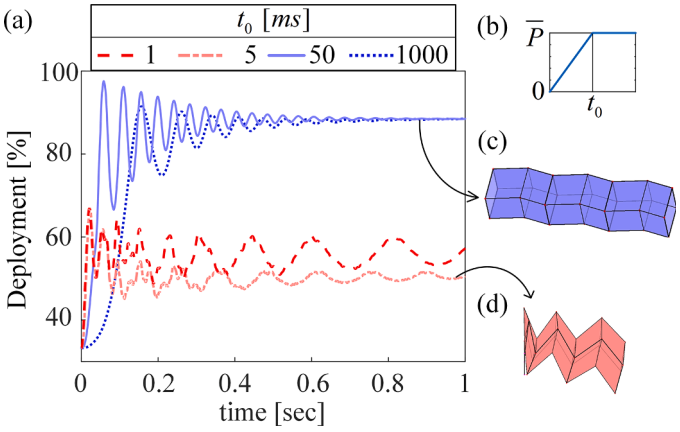

Fig. 11. (a) Time history of the dynamic deployment under different rates of pressurization. The stiffness parameters are $[\bar{r}_k = 10,\ \bar{k}_f/\bar{k}_{f0} = 1]$. The final value of the pressure magnitude is $\overline{P}/\overline{P}_0 = 20$. (b) We define the pressurization rate by the time t_0. (c-d) The settled configurations of the dynamic deployment under t_0= 50 and 5 ms, respectively.

Conversely, applying pressure more slowly results in the structure approximately maintaining the rigid folding path, exhibiting some axial oscillation but ultimately stabilizing with minimal distortion, as illustrated in Fig. 11c.

Given the influence of both pressurization rate and final pressure magnitude on dynamic deployment behaviors, we examine the dynamic deployment under a ramped pressure application by adjusting these two variables, as depicted in Fig. 12. The contour plots in Fig. 12a categorize the dynamic deployment into three categories, depending on the pressure field parameters, with their time histories presented in Fig. 12b. In scenarios where the pressurization rate is sufficiently high, represented

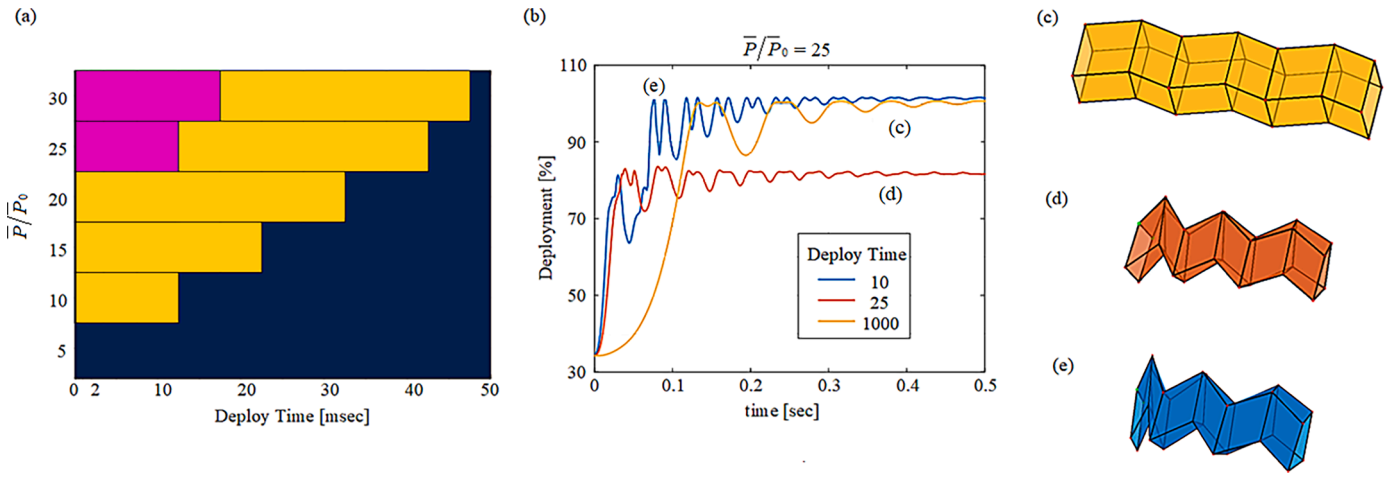

Fig. 12. (a) Three dynamic deployment paths are represented by colored regions in the parameter space, with the y-axis showing the ending pressure magnitude and the x-axis showing the time to achieve it. The blue region indicates smooth deployment, the yellow region corresponds to snap-through leading to a distorted stable equilibrium, and the magenta region represents snap-through followed by a return to a minimally distorted configuration. (b) Time histories of three typical dynamic deployment paths at the same ending pressure magnitude but with different deployment times. (c, d, e) Snapshots of the dynamic configurations during the three deployment processes shown in (b): (c) the final configuration for the yellow curve, (d) the final distorted configuration for the red curve, and (e) the intermediate snap-through configuration for the blue curve.

by the magenta region, the structure undergoes a snap-through into a distorted form before snapping back, as illustrated in Fig. 12e and indicated by the blue curve in the time history of Fig. 12b. Within a specific range of pressurization rates, the structure snaps into a distorted state and remains there without further deployment, as shown in Fig. 12d. When the pressurization rate is slow enough, the structure will deploy without significant distortion, represented by the dark blue region in Fig. 12a, and illustrated by the yellow curve in Fig. 12b. This demonstrates how, for a given final pressure magnitude, the structure may follow varied dynamic deployment paths depending on the pressurization rate.

7. Proof of concept prototypes and future work

Given the comprehensiveness of our analysis studies and rich outcomes, experimental efforts are not in the scope of this current paper. We will address them in our future work, which will deepen our understanding of the dynamic behavior of origami structures and further validate the practical efficacy of our ideas and findings. However, in this section, we present a proof-of-concept prototype to demonstrate the configurations corresponding to the multiple stable equilibria discussed in Section 5. Additionally, we introduce 3D-printed prototypes designed for our future dynamic tests with pressurization.

To qualitatively verify the phenomena observed in the numerical simulations of a three-unit Miura origami tube, we constructed an

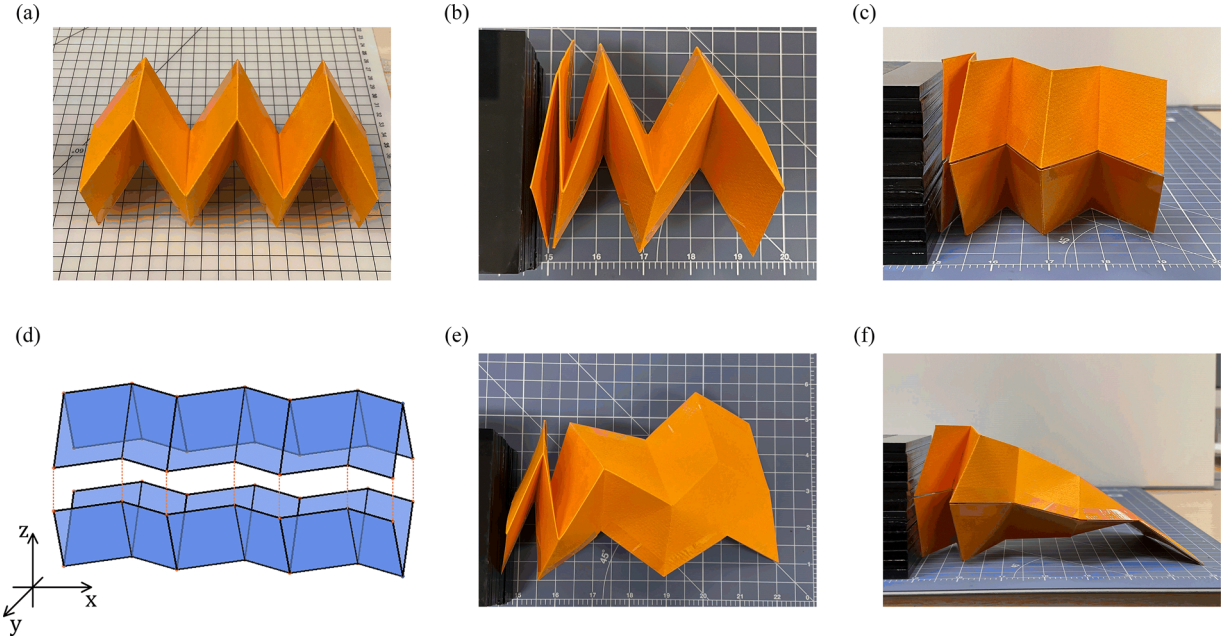

Fig. 13. Proof-of-concept paper prototypes. (a) Configuration corresponding to the first stable equilibrium, characterized by major deformation at the fold creases. (b, c) Configuration corresponding to the second stable equilibrium branch as shown in Fig. 9(b-d). (b) Top view in the x-y plane as defined in (d); (c) Front view in the x-z plane as defined in (d). (e, f) Configuration corresponding to the second settled state shown in Fig. 8(f-h). (e) Top view in the x-y plane as defined in (d); (f) Front view in the x-z plane as defined in (d).

origami tube prototype, as shown in Fig. 13. The prototype was made by folding two hardboard sheets to form the upper and lower origami panels, which were then connected using adhesive tape to create the tube structure (see Fig. 13(d) or Fig. 1(c, d)). The fold creases were created using dashed cuts with a laser cutter. Based on the stiffness analysis in Section 2.2 and the non-dimensionalization scheme in Section 2.4, using material constants derived for paper-folded origami structures [83], we estimated the stiffness parameters for this paper prototype. The non-dimensionalized folding stiffness is $\overline{k}_f = 2.48 \times 10^{-5}$, and the ratio of this crease folding stiffness to the nominal non-dimensionalized stiffness is $\overline{k}_f/\overline{k}_{f0} = 1.1$. The ratio between facet bending and crease folding stiffness is $\overline{k}_b/\overline{k}_f = 10$. Both ratios are closely aligned with the values used in the numerical simulations shown in Fig. 9. This prototype successfully replicated multiple stable equilibrium configurations, consistent with the analytical studies, as demonstrated in Fig. 13a-c, e, and f).

Our findings indicate that, in origami structures with relatively low panel stiffness—due to either panel geometry or the base material—bending and stretching deformations become nontrivial. These deformations result in multiple stable equilibria with significantly different overall configurations, highlighting the necessity of considering panel deformation in dynamics. This understanding of the multistability of origami structures is crucial, as it influences the dynamics of origami deployment. Additionally, the prototype in Fig. 13 is unpressurized, corresponding to a zero-pressure state, suggesting that the origami structure, under given construction material and geometry, could maintain various stable equilibria across a wider range of the pressure fields.

Previous research has demonstrated that origami structures can achieve advanced, controllable, and adaptive reconfiguration through fluidic control [17,23,65]. Although challenging, it has been shown that pressurization and airtightness can be achieved with proper design [55, 64]. Building on these findings, we have explored prototype fabrication by manufacturing 3D-printed models, as shown in Fig. 14. In Fig. 14 (e-h), we present a 3D-printed prototype with drilled holes in the end caps. These holes allow for the dissolution of internal support materials and provide openings for air pumping. The polygonal end caps, based on Tachi's design [88], accommodate shape changes in the cross sections of the origami tube during deployment. For these two prototypes, we used TPU-95A as the 3D printing material [89].

Similar to the paper prototype, using material constants sourced from the manufacturer's website [89], we can estimate the stiffness parameters of this model. The non-dimensionalized folding stiffness is $\overline{k}_f = 7.10 \times 10^{-5}$, and the ratio of this crease folding stiffness to the nominal non-dimensionalized stiffness is $\overline{k}_f/\overline{k}_{f0} = 3.17$. The ratio between facet bending and crease folding stiffness is $\overline{k}_b/\overline{k}_f = 10$. These parameters remain close (within one order of magnitude) to those used in Fig. 9. According to Fig. 10e, this structure could exhibit three distinct stable equilibria and demonstrate snap-through and snap-back behavior.

Building upon our findings and prototypes, we propose the following elements and directions for future work in experimental validations:

a) Material Selection: It would be important to explore various materials for the origami prototypes using 3D printing technology. Different materials will help us understand the impact of material properties on the dynamic behavior of the origami structures.
b) Pressurization: Different approaches to seal the ends of the origami tube should be investigated. For instance, experiments should compare polygonal caps and membranes to achieve effective sealing.
c) Dynamic Testing: With these advanced prototypes, we will conduct dynamic tests to explore various deployment behaviors. These tests will help us observe the real-time dynamic responses of the pressurized origami tubes.
d) Validation: Finally, the numerical simulation results would be validated both qualitatively and quantitatively. This validation process will involve comparing experimental data with simulation predictions to ensure the accuracy and reliability of our approach.

8. Conclusions

In this paper, we investigated the deployment dynamics of fluidic Miura origami tubular structures. Our primary contributions include the development of a novel dynamic model that integrates panel inertia and flexibility, offering a perspective on the dynamics of tubular origami

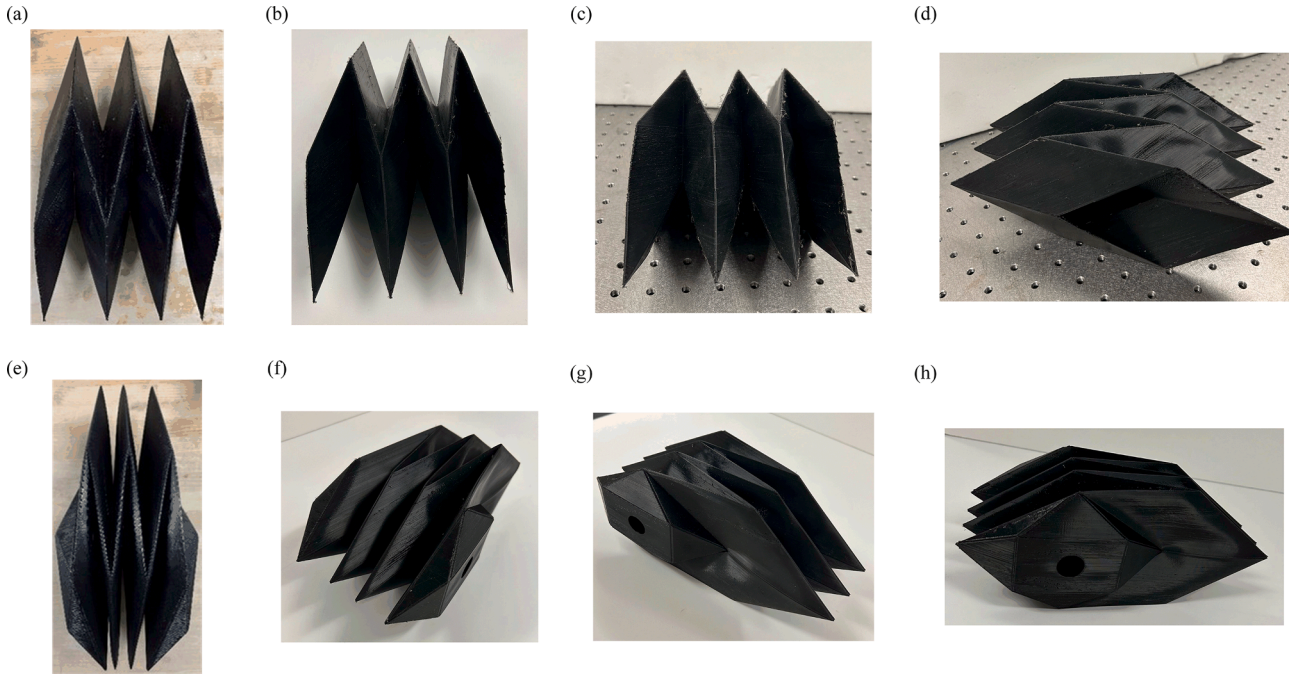

Fig. 14. Two 3D printed prototypes for dynamic tests with pressurization. (a-d) Prototype with two open ends. (e-h) Prototype with both ends closed using polygonal caps.

deployment via pressurization—a topic that has not been previously explored. We employed quasi-static and eigen analyses to examine the structural characteristics of pressurized origami tubes, identifying unique dynamic responses through numerical simulations and further exploring these responses through a multi-stability landscape analysis. We also demonstrated the ability to tailor deployment behaviors by modulating the pressure field, including adjustments to both the magnitude and rate of pressurization. This new knowledge is critically important for expanding the design space and acknowledging the influence of dynamics in deployable structures.

Our model successfully captures key panel deformations in origami structures, the stretching and bending, which have not been addressed in existing models for dynamic analysis. Quasi-static studies reveal that folding stiffness significantly influences deployment at lower pressure levels. As pressure increases, the length of the origami tube stabilizes at an 89% deployment stage, which corresponds to the maximum volume configuration achievable under the assumption of rigid panels. Prior to reaching this 89% threshold, the structure primarily deforms through crease folding, following a path of least energy. Beyond this configuration, the origami tube transitions to a panel stretching mode to sustain a greater volume configuration in response to increasing pressure. Eigen analysis indicates that the effective stiffness of the origami tube rises with increasing pressure, suggesting that fluidic origami tubes offer the potential to tailor deployment performance through pressure modulation. These altered structural properties create a promising new design space for adaptive origami structures governed by fluidic control.

Our dynamic analysis, for the first time, categorizes three distinct deployment behaviors influenced by pressure amplitude, which stem from the intrinsic nonlinearity of origami structures. A key contribution is the discovery of a markedly different stable state accessed via a snap-through behavior during dynamic deployment under certain pressure conditions. Furthermore, the origami tube can revert to its original configuration if the applied pressure is sufficiently high, exhibiting a snap-back behavior. These snap-through and snap-back dynamics arise when the structure overcomes its energy barrier with energy supplied by the applied pressure field. This phenomenon is governed by the multi-stability landscape of the origami structure, and our investigation has significant contribution in showing that the number and nature of stable states can be controlled by varying the fluidic pressure and structural stiffness. The intricate coupling between the pressure field and the nonlinear characteristics of the origami structure suggests a vast area for further exploration within the multi-stability landscape of fluidic origami tubular structures.

Additionally, our research reveals that the rate of pressurization, in addition to the magnitude, has a qualitative impact on the deployment path. An increased pressurization rate can induce the same snap-back behavior as an increase in pressure magnitude, emphasizing the potential for fine-tuning deployment dynamics through fluidic control. This finding broadens the scope of future research, underscoring the adaptability and controllability of fluidic pressurization in influencing strain energy and deployment behavior.

Overall, the methodologies and insights derived from this study contribute to the creation of a framework for designing desired deployment dynamics (e.g., rapid and smooth transitions) and final configurations or intentional reconfigurations of fluidic origami tubular structures. The novel outcomes of this research are valuable for raising awareness and understanding of new phenomena that canot be observed in past studies, such as highly distorted stable configurations and their snap-through or snap-back behaviors. Additionally, this study offers original guidelines for designing origami structures with specific parameters, including material properties, pattern geometry, and operating conditions such as pressure level and rate, thereby expanding the potential for innovation in the field of fluidic origami and deployable structures.

CRediT authorship contribution statement

Yutong Xia: Writing – review & editing, Writing – original draft, Visualization, Validation, Methodology, Investigation, Formal analysis, Data curation. **Evgueni Filipov:** Writing – review & editing, Supervision, Resources, Project administration, Methodology, Investigation, Funding acquisition, Formal analysis, Conceptualization. **K.W. Wang:** Writing – review & editing, Visualization, Validation, Supervision, Software, Resources, Project administration, Methodology, Investigation, Funding acquisition, Formal analysis, Data curation, Conceptualization.

Declaration of competing interest

The authors declare that they have no known competing financial interests or personal relationships that could have appeared to influence the work reported in this paper.

Acknowledgements

We appreciate the funding support from the Ford-University of Michigan Alliance Framework and the National Science Foundation (NSF) Grant CMMI #1634545. The second author acknowledges funding from NSF Grant CAREER #1943723. The authors are grateful to Janice Tardiff and Chaitanya Nimmagadda from the Ford Motor Company, for many helpful discussions regarding this work.

Appendix

The total strain energy V consists of contributions from crease folding (V_{fold}), panel bending (V_{bend}), and panel stretching ($V_{stretch}$). The strain energy from crease folding V_{fold}, results from bending of torsional hinges at folding creases. The panel bending strain energy V_{bend}, is due to bending of the torsional hinges at bend lines in the model. Finally, the strain energy from stretching in the panels $V_{stretch}$, is due to elongation and compression of bars. Strain energy from crease folding or panel bending is computed by

$$V_i = \sum_i \int_{\theta_0}^{\theta} M(\widehat{\theta}_i) d\widehat{\theta}_i, \ (i = fold, bend), \tag{A.1}$$

$$F_i = \frac{\partial V_i}{\partial x} = \sum_i \frac{\partial V_i}{\partial \theta_i} \frac{\partial \theta_i}{\partial x} = \sum_i M(\theta_i) \frac{\partial \theta_i}{\partial x}, \ (i = fold, \ bend), \tag{A.2}$$

where θ_i can be the folding angle θ_f or the bending angle θ_b, and M is the reactive torque. The force generated on related nodes from the torque M is calculated by Equation (A.2). Each dihedral angle θ_i is formed by its two adjacent triangular panels, containing a total of four nodes, therefore the partial derivative $\partial\theta_i/\partial x$ results in four vectors.

Based on the strain energy from panel stretching $V_{stretch}$, calculated by

$$V_{stretch} = \sum_{s=bar} \int_0^{L_{bar}} W(E_s) A_{s\_bar} dx, \tag{A.3}$$

$$W(E) = \sum_{i=1}^{N} \frac{\mu_i}{\alpha_i} (\lambda_1^{\alpha_i} - 1), \tag{A.4}$$

$$\lambda_1 = \sqrt{2E + 1}, \tag{A.5}$$

where W is the strain energy density function, E is the Green-Lagrange strain tensor, α_i,μ_i,N are material constants, and λ_1 is axial stretch, we derived the corresponding nodal force F_s by

$$F_s = \frac{\partial V_{stretch}}{\partial x}. \tag{A.6}$$

Our dynamic model considers damping due to crease folding and panel elastic deformations, including the panel bending and stretching, corresponding to $D(\dot{x})$ in Eq. (7). The damping from crease folding and panel bending are represented by damping at hinges in the bar and hinge model with equivalent linear damping coefficient c_f (crease folding) and c_b (panel bending). The nodal force F_{di} of damping from crease folding or panel bending is derived by

$$F_{di} = c_i \dot{\theta} \frac{\partial \dot{\theta}}{\partial \dot{x}} \ (i = fold, bend), \tag{A.7}$$

where the angular velocity $\dot{\theta}$ is a function of the dihedral angle in the hinge (θ) and the translational velocity $\dot{x}$: $\dot{\theta} = \frac{d}{dt}\theta(x) = \frac{d\theta}{dx}\frac{dx}{dt}$. The damping from panel stretching is represented by damping of bar deformation in the bar and hinge model with equivalent linear damping coefficient c_{vs}. The nodal force F_{ds} from panel stretching is calculated by

$$F_{ds} = c_{vs} \dot{l} \frac{\partial l}{\partial x}, \tag{A.8}$$

where l is the length of a bar, and $\dot{l}$ is the rate of length change of the bar.

The kinetic energy $T(x, \dot{x})$ is computed by a summation of kinetic energy of each individual node

$$T = \sum_i \frac{1}{2} m_i \dot{x}_i^2 \tag{A.9}$$

where m_i is the mass of the i-th node, and $\dot{x}_i$ is its nodal linear velocity.

Data availability

Data will be made available on request.

References

[1] Suto K, Noma Y, Tanimichi K, Narumi K, Tachi T. Crane: an Integrated Computational Design Platform for Functional, Foldable, and Fabricable Origami Products. ACM Trans Comput-Hum Interact 2023;30(4):52. https://doi.org/10.1145/3576856. Articlepages.

[2] Lang RTwists. Tilings, and tessellations: mathematical methods for geometric origami. Boca Raton, FL: CRC Press; 2018.

[3] Imada, R., Hull, T.C., Ku, J.S., Tachi, T. Nonlinear kinematics of recursive origami inspired by the spidron. 2024. arXiv:2403.09278. https://arxiv.org/abs/2403.09278.

[4] Yang J, You Z. Folding miura-ori of uniform thickness with one degree-of-freedom. ASME J Mech Robot 2024;16(11):111004. https://doi.org/10.1115/1.4065004.

[5] Dong Z, Zhu Y, Guo X. A general simulation method for complex deformation of irregular-shaped origami configurations. Acta Mech Solida Sin 2024;37:90–8. https://doi.org/10.1007/s10338-023-00443-7.

[6] Micheletti A, Tiero A, Tomassetti G. Simulation and design of isostatic thick origami structures. Meccanica 2024. https://doi.org/10.1007/s11012-024-01815-0.

[7] Langford T, Mohammed A, Essa K, Elshaer A, Hassanin H. 4D printing of origami structures for minimally invasive surgeries using functional scaffold. Appl Sci 2021;11:332. https://doi.org/10.3390/app11010332.

[8] Rogers J, Huang Y, Schmidt OG, Gracias DH. Origami MEMS and NEMS. MRS Bull 2016;41(2):123–9.

[9] Li S, Fang H, Sadeghi S, Bhovad P, Wang KW. Architected origami materials: how folding creates sophisticated mechanical properties. Adv Mater 2019;31:1805282. https://doi.org/10.1002/adma.201805282.

[10] Lebee A. From folds to structures, A review. Int J Space Struct 2015;30(2):55–74.

[11] Zhu Y, Filipov ET. Large-scale modular and uniformly thick origami-inspired adaptable and load-carrying structures. Nat Commun 2024;15:2353. https://doi.org/10.1038/s41467-024-46667-0.

[12] Shah SIH, Bashir S, Ashfaq M, Altaf A, Rmili H. Lightweight and low-cost deployable origami antennas—a review. IEEE Access 2021;9:86429–48. https://doi.org/10.1109/ACCESS.2021.3088953.

[13] Lang RJ, Magleby S, Howell L. Single degree-of-freedom rigidly foldable cut origami flashers. ASME J Mech Rob 2016;8(3):031005.

[14] Bolanos D, Varela K, Sargent B, Stephen MA, Howell LL, Magleby SP. S.electing and optimizing origami flasher pattern configurations for finite-thickness deployable space arrays. ASME J Mech Des 2023;145(2):023301. https://doi.org/10.1115/1.4055900.

[15] Kaddour A-S, Velez CA, Hamza M, Brown N, Ynchausti C, Magleby SP, Howell L, Georgakopoulos SV. A. Foldable and reconfigurable monolithic reflect array for space application. IEEE Access 2020;8:219355–66.

[16] Xu Q, Gu L, Liu Z, Zhang L, Yuan J, Lu C, Lei K, Du Z. Design, preparation and characterization of three-dimensional auxetic warp and weft backed weave fabrics based on origami tessellation structures. Textile Res J 2022. https://doi.org/10.1177/00405175221094044.

[17] Li S, Wang KW. Fluidic origami: a plant-inspired adaptive structure with shape morphing and stiffness tuning. Smart Mater Struct 2015;24(10):105031.

[18] Fang H, Li S, Ji H, Wang KW. Uncovering the deformation mechanisms of origami metamaterials by introducing generic degree-four vertices. Phys Rev E 2016;94(4):1–11.

[19] Fang H, Li S, Wang KW. Self-locking degree-4 vertex origami structures. Proc R Soc A Math Phys Eng Sci 2016;472(2195):20160682.

[20] Fang H, Chu SA, Xia Y, Wang KW. Programmable self-locking origami mechanical metamaterials. Adv Mater 2018;30(15):1706311.

[21] Filipov ET, Tachi T, Paulino GH. Origami tubes assembled into stiff, yet reconfigurable structures and metamaterials. Proc Natl Acad Sci U S A 2015;112(40):12321–6. https://doi.org/10.1073/pnas.1509465112.

[22] Sadeghi S, Li S. Dynamic folding of origami by exploiting asymmetric bi-stability. Extreme Mech Lett 2020;40:100958. https://doi.org/10.1016/j.eml.2020.100958.
[23] Li S, Wang KW. Fluidic origami with embedded pressure dependent multi-stability: a plant inspired innovation. J R Soc Interface 2015;12(111):20150639.
[24] Li S, Fang H, Wang KW. Recoverable and programmable collapse from folding pressurized origami cellular solids. Phys Rev Lett 2016;117(11):1–5.
[25] Woodruff SR, Filipov ET. Curved creases redistribute global bending stiffness in corrugations: theory and experimentation. Meccanica 2021;56:1613–34. https://doi.org/10.1007/s11012-020-01200-7.
[26] Filipov ET, Paulino GH, Tachi T. Deployable sandwich surfaces with high out-of-plane stiffness. J Struct Eng 2019;145(2):04018244. https://doi.org/10.1061/(ASCE)ST.1943-541X.0002240.
[27] Fang H, Wang KW, Li S. Asymmetric energy barrier and mechanical diode effect from folding multi-stable stacked-origami. Extreme Mech Lett 2017;17:7–15. https://doi.org/10.1016/j.eml.2017.09.008.
[28] Sengupta S, Li S. Harnessing the anisotropic multistability of stacked-origami mechanical metamaterials for effective modulus programming. J Intell Mater Syst Struct 2018;29(14):2933–45.
[29] Hanna BH, Lund JM, Lang RJ, Magleby SP, Howell LL. Waterbomb base: a symmetric single-vertex bistable origami mechanism. Smart Mater Struct 2014;23(9).
[30] Filipov ET, Redoutey M. Mechanical characteristics of the bistable origami hypar. Extreme Mech Lett 2018;25:16–26. https://doi.org/10.1016/j.eml.2018.10.001.
[31] Sadeghi S, Allison SR, Bestill B, Li S. TMP origami jumping mechanism with nonlinear stiffness. Smart Mater Struct 2021;30:065002.
[32] Kaufmann J, Bhovad P, Li S. Harnessing the Multistability of Kresling origami for reconfigurable articulation in soft robotic arms. Soft Robot 2022;9(2):212–23. https://doi.org/10.1089/soro.2020.0075.
[33] Tao J, Li S. A study of the multi-stability in a non-rigid stacked miura-origami cellular mechanism. In: Proc. ASME IDETC, 2021; Volume 8B: 45th Mechanisms and Robotics Conference (MR). Virtual; 2021. August 17–19V08BT08A033.
[34] Liu K, Tachi T, Paulino GH. Invariant and smooth limit of discrete geometry folded from bistable origami leading to multistable metasurfaces. Nat Commun 2019;10:4238. https://doi.org/10.1038/s41467-019-11935-x.
[35] Li Z, Agarwal V, Wang L, Wang KW. On-demand tuning of mechanical stiffness and stability of Kresling origami harnessing its nonrigid folding characteristics. Smart Mater Struct 2023;32(8):085025. https://doi.org/10.1088/1361-665X/ace0eb.
[36] Liu Z, He Z, Hu X, Sun Z, Ge Q, Xu J, Fang H. Origami-enhanced mechanical properties for worm-like robot. Soft Robot 2023. https://doi.org/10.1089/soro.2023.0246.
[37] Li Z, Kidambi N, Wang L, Wang KW. Uncovering rotational multifunctionalities of coupled Kresling modular structures. Extreme Mech Lett 2020;39:100795. https://doi.org/10.1016/j.eml.2020.100795.
[38] Yu Y, Hong TK, Economou A, Paulino GH. Rethinking origami: a generative specification of origami patterns with shape grammars. Comput. Aided Des. 2021;137:103029. https://doi.org/10.1016/j.cad.2021.103029.
[39] Zhu Y, Filipov ET. Harnessing interpretable machine learning for origami feature design and pattern selection. ArXiv 2022. https://doi.org/10.48550/ARXIV.2204.07235.
[40] Misseroni D, Pratapa P, Liu K, Paulino GH. Experimental realization of tunable Poisson's ratio in deployable origami metamaterials. Extreme Mech Lett 2022;53:101685. https://doi.org/10.1016/j.eml.2022.101685.
[41] Pratapa P, Liu K, Vasudevan SP, Paulino GH. Reprogrammable kinematic branches in tessellated origami structures. ASME. J. Mech. Rob. 2021;13(3):031004. https://doi.org/10.1115/1.4049949.
[42] Zhu Y, Schenk M, Filipov ET. A Review on Origami Simulations From Kinematics, To Mechanics, Toward Multiphysics. Appl Mech Rev 2022;74(3):030801.
[43] Thota M, Wang KW. R.econfigurable origami sonic barriers with tunable bandgaps for traffic noise mitigation. J Appl Phys 2017;122(15).
[44] Thota M, Li S, Wang KW. L.attice reconfiguration and phononic band-gap adaptation via origami folding. Phys Rev B 2017;95(6):1–10.
[45] Wo Z, Raneses JM, Filipov ET. Locking zipper-coupled origami tubes for deployable energy absorption. ASME J Mech Rob 2022;14(4):041007. https://doi.org/10.1115/1.4054363.
[46] Wang H, Zhao D, Jin Y, Wang M, You Z, Yu G. Study of collapsed deformation and energy absorption of polymeric origami-based tubes with viscoelasticity. Thin-Walled Struct 2019;144:106246. https://doi.org/10.1016/j.tws.2019.106246.
[47] Gattas JM, You Z. Quasi-static impact of indented foldcores. Int J Impact Eng 2014;73:15–29.
[48] Yuan L, Shi H, Ma J, You Z. Quasi-static impact of origami crash boxes with various profiles. Thin-Walled Struct 2019;141:435–46. https://doi.org/10.1016/j.tws.2019.04.028.
[49] Fang H, Li S, Ji H, Wang KW. Dynamics of a bistable Miura-origami structure. Phys Rev E 2017;95(5):052211.
[50] Ishida S, Uchida H, Shimosaka H, Hagiwara I. Design and numerical analysis of vibration isolators with quasi-zero-stiffness characteristics using bistable foldable structures. J Vib Acoust Trans ASME 2017;139(3):031015.
[51] Ishida S, Suzuki K, Shimosaka H. Design and experimental analysis of origami-inspired vibration isolator with quasi-zero-stiffness characteristic. J Vib Acoust 2017;139(5):051004.
[52] Sadeghi S, Li S. Fluidic origami cellular structure with asymmetric quasi-zero stiffness for low-frequency vibration isolation. Smart Mater Struct 2019;28(6).
[53] Agarwal V, Wang KW. O.n the nonlinear dynamics of a Kresling-pattern origami under harmonic force excitation. Extreme Mech Lett 2022;52:101653. https://doi.org/10.1016/j.eml.2022.101653.
[54] Bhovad P, Li S. Physical reservoir computing with origami and its application to robotic crawling. Sci Rep 2021;11:13002. https://doi.org/10.1038/s41598-021-92257-1.
[55] Khosravi H, Iannucci SM, Li S. Pneumatic soft actuators with Kirigami skins. Front Robot AI 2021;8:749051. https://doi.org/10.3389/frobt.2021.749051.
[56] Ze Q, Wu S, Nishikawa J, Dai J, Sun Y, Leanza S, Zemelka C, Novelino LS, Paulino GH, Zhao R. Soft robotic origami crawler. Sci Adv 2022;8(13). https://doi.org/10.1126/sciadv.abm7834.
[57] Wu S, Ze Q, Dai J, Udipi N, Paulino GH, Zhao R. Stretchable origami robotic arm with omnidirectional bending and twisting. Proc Natl Acad Sci USA 2021;118(36). https://doi.org/10.1073/pnas.2110023118.
[58] Filipov ET, Paulino GH, Tachi T. Origami tubes with reconfigurable polygonal cross-sections. Proc R Soc A Math Phys Eng Sci 2016;472(2185):20150607.
[59] Filipov ET, Tachi T, Paulino GH. C.oupled origami tubes for stiff deployable cantilevers. In: Proc. ASME IDETC; 2019. V05BT07A023.
[60] Rus D, Tolley MT. D.esign, fabrication and control of origami robots. Nat Rev Mater 2018;3(6):101–12.
[61] Jin L, Forte AE, Deng B, Rafsanjani A, Bertoldi K. Kirigami-Inspired Inflatables with Programmable Shapes. Adv Mater 2020;32(33):1–7.
[62] Peraza-Hernandez EA, Hartl DJ, Malak RJ, Lagoudas DC. O.rigami-inspired active structures: a synthesis and review. Smart Mater Struct 2014;23(9):094001.
[63] Khosravi H, Iannucci SM, Li S. Pneumatic soft actuators with Kirigami skins. Front Robot AI 2021;8:749051. https://doi.org/10.3389/frobt.2021.749051.
[64] Zhang Q, Tan K, He Z, Pang H, Wang Y, Fang H. An origami continuum manipulator with modularized design and hybrid actuation: accurate kinematic modeling and experiments. Adv Intell Syst 2024;6:2300468. https://doi.org/10.1002/aisy.202300468.
[65] Wu SR, Chen TH, Tsai HY. A review of actuation force in origami applications. J Mech 2019;35(5):627–39. https://doi.org/10.1017/jmech.2019.21.
[66] Leanza S, Wu S, Sun X, Qi HJ, Zhao RR. Active materials for functional origami. Adv Mater 2024;36:2302066. https://doi.org/10.1002/adma.202302066.
[67] Georgakopoulos SV, et al. Origami antennas. IEEE Open J Antennas Propag 2021;2:1020–43. https://doi.org/10.1109/OJAP.2021.3121102.
[68] Sane H, Bhovad P, Li S. Actuation performance of fluidic origami cellular structure: a holistic investigation. Smart Mater Struct 2018;27(11):115014.
[69] Grey SW, Schenk M, Scarpa FL. Local actuation of tubular origami. Proc Seventh Meet Origami Sci Math Educ 2018.
[70] Grey SW, Scarpa F, Schenk M. Strain reversal in actuated origami structures. Phys Rev Lett 2019;123(2):025501.
[71] Kidambi N, Wang KW. Dynamics of Kresling origami deployment. Phys Rev E 2020;101(6):063003.
[72] Liu Z, Zhang X, Wang KW, Xu J, Fang H. Data-driven modeling of multi-stable origami structures: extracting the global governing equation and exploring the complex dynamics. Mech Syst Signal Process. 2024;220:111659. https://doi.org/10.1016/j.ymssp.2024.111659.
[73] Wu H, Fang H, Chen L, Xu J. Transient dynamics of a miura-origami tube during free deployment. Phys Rev Appl 2020;14:034068.
[74] Wang C, Zhang D, Li J, Li Y, Zhang X. Deployment dynamics of thick panel Miura-origami. Aerosp Sci Technol 2024;144:106246.
[75] Rodrigues GV, Savi MA. N.onlinear dynamics and chaos of a waterbomb origami unit-cell considering different symmetry conditions. Mech Res Commun 2024;136:104233.
[76] Zou Y, Feng F, Liu K, Lv P, Duan H. Kinematics and dynamics of non-developable origami. Proc R Soc A Math Phys Eng Sci 2023;480. https://doi.org/10.1098/rspa.2023.0610.
[77] Yu X, Wang L. Nonlinear dynamics of coupled waves in Kresling origami metamaterials. J Sound Vib 2024;577:118263.
[78] Xia Y, Kidambi N, Filipov ET, Wang KW. D.eployment dynamics of Miura origami sheets. J Comput Nonlinear Dyn 2022;17(7):071005.
[79] Hu YC, Zhou YX, Kwok KW, et al. Simulating flexible origami structures by finite element method. Int J Mech Mater Des 2021;17:801–29. https://doi.org/10.1007/s10999-021-09538-w.
[80] Yuan T, Tang L, Liu Z, et al. Nonlinear dynamic formulation for flexible origami-based deployable structures considering self-contact and friction. Nonlinear Dyn 2021;106:1789–822. https://doi.org/10.1007/s11071-021-06860-y.
[81] Liu, K., Paulino, G.H. M.ERLIN: a MATLAB implementation to capture highly nonlinear behavior of non-rigid origami. 2016. https://api.semanticscholar.org/CorpusID:52995011.
[82] Liu K, Paulino GH. H.ighly efficient nonlinear structural analysis of origami assemblages using the MERLIN2 software. Merlin 2018;2.
[83] Filipov ET, Liu K, Tachi T, Schenk M, Paulino GH. B.ar and hinge models for scalable analysis of origami. Int J Solids Struct 2017;124:26–45.
[84] Liu K, Paulino GH. N.onlinear mechanics of non-rigid origami: an efficient computational approach. Proc R Soc A Math Phys Eng Sci 2018;474:20180087.
[85] Woodruff SR, Filipov ET. A bar and hinge model formulation for structural analysis of curved-crease origami. Int J Solids Struct 2020;204–205:114–27. https://doi.org/10.1016/j.ijsolstr.2020.08.010.

[86] Zhu Y, Filipov ET. A bar and hinge model for simulating bistability in origami structures with compliant creases. ASME J Mech Rob 2020;12(2):021110. https://doi.org/10.1115/1.4045955.
[87] Zhu Y, Filipov ET. An efficient numerical approach for simulating contact in origami assemblages. Proc R Soc A Math Phys Eng Sci 2019;475:20190366. https://doi.org/10.1098/rspa.2019.0366.
[88] Tachi T. In: Proceedings of IASS Annual Symposia, IASS 2017 Hamburg Symposium: Deployable Structures & Origami. International Association for Shell and Spatial Structures (IASS); 2017. p. 1–10.
[89] Ultimaker. TPU 95A material properties. Ultimaker; 2024. https://ultimaker.com/materials/tpu-95a.